Chemical Science

ROYAL SOCIETY OF CHEMISTRY

EDGE ARTICLE

View Article Online
View Journal | View Issue

Open Access Article. Published on 06 March 2023. Downloaded on 1/11/2026 4:22:25 PM.
This article is licensed under a Creative Commons Attribution-NonCommercial 3.0 Unported Licence.

Check for updates

Cite this: *Chem. Sci.*, 2023, **14**, 3982

All publication charges for this article have been paid for by the Royal Society of Chemistry

Molybdenum chloride double perovskites: dimensionality control of optical and magnetic properties†

Devesh Chandra Binwal,[a] Prashurya Pritam Mudoi,[a] Debendra Prasad Panda[b] and Pratap Vishnoi *[a]

Received 9th January 2023
Accepted 3rd March 2023

DOI: 10.1039/d3sc00132f

rsc.li/chemical-science

Halide double perovskites are a promising class of semiconducting materials for applications in solar cells and other optoelectronic devices. Recently, there has been a surge of interest in these materials to study phenomena beyond optoelectronics, especially magnetism. Here, we report three new Mo^{3+} ($4d^3$) based chloride double perovskites: a 3-D rock-salt ordered $Cs_2NaMoCl_6$, a 1-D chain $(MA)_2AgMoCl_6$ and a Dion–Jacobson type 2-D layered $(1,4\text{-BDA})_2AgMoCl_8$ (MA = methylammonium; 1,4-BDA = 1,4-butanediammonium). Their structures and dimensionalities can be tuned by means of the A-cation. The measured bandgaps are relatively narrow (2.0–2.1 eV) which show a blueshift on reducing the dimensionality. At low temperatures, we observe antiferromagnetic coupling between the nearest-neighbour Mo^{3+} ions in all these systems. $Cs_2NaMoCl_6$ shows stronger coupling with a frustration index *f* of 5 which we attribute to the geometrically frustrating fcc lattice of Mo^{3+} ions. This work expands the scope of halide double perovskites beyond main group metals and beyond optoelectronics, and we hope that it will lead to future developments in magnetic halide perovskites.

1. Introduction

Halide double perovskites (HDPs) (also known by their alternative name, elpasolite) are typically a class of quaternary compounds of composition $A_2B^IB^{III}X_6$ (A = A-site monocation; B^I = B-site monovalent metal; B^{III} = B-site trivalent metal; X = halide). At the six-coordinated B-site, B^I and B^{III} metal ions show rock-salt ordering, which is often driven by their charge difference.[1] In some cases, such as $Cs_2Hg^{II}M^{II}Cl_6$ (M^{II} = Cu or Pd), coordination geometry can drive the B-site metal ordering even though the charge difference is zero.[2] The inorganic lattice of $A_2B^IB^{III}X_6$ could be constructed by transmutation of two divalent metal ions (B^{II}) of a $AB^{II}X_3$ single perovskite into one B^I ion and one B^{III} ion, *i.e.* $2B^{II} \rightarrow B^I + B^{III}$.[3] The interest in HDPs began to surge in 2016, when three research groups independently reported the synthesis and the optoelectronic properties of Cs_2AgBiX_6 (X = Cl, Br).[1,4,5] Since then, many such materials have been realized, thanks to the rich degree of freedom in selecting B^I and B^{III} metals. Most of the HDPs of current interest are based on post-transition metals with a $d^{10}s^2$ configuration (such as Sb[6] and Bi[7]) or $d^{10}s^0$ configuration (such as In[8]) at the B^{III} site and any size-matching monovalent metals (such as Ag, Tl, Na, and K) at the B^I site, and have been widely reported for use in photovoltaics,[9] X-ray detectors,[10] photodetectors,[11] and humidity sensors.[12] Unfortunately, they have their own limitations mainly due to large band gaps and large effective carrier masses.[13,14]

During the 1970s to the 1990s, a number of fluoride double perovskites of trivalent 3d metal ions,[15–19] and some 4d metal ions such as Mo,[20,21] and Rh,[22] were reported. Rare-earth metals were also incorporated in fluoride based double perovskites.[23,24] At that time, particular interest was focused on synthesis and structures, and in some cases magnetism. In light of the recent surge of interest in semiconducting halide perovskites, there have been reports on incorporating transition metals at the perovskite B-site with the intention to develop novel perovskites with high potential to be used in emerging applications such as spin-electronics, where exchange interaction between unpaired spins is important.[25–28] $Fe^{III}(3d^5)$,[29] and Ru^{III} $(4d^5)$[30] have been alloyed into the benchmark double perovskite $Cs_2AgBiBr_6$ to decrease its bandgap by introducing an intermediate band inside the pristine bandgaps. Recently, Ning *et al.* reported interesting magnetic exchange properties in Fe-alloyed $Cs_2AgBiBr_6$ and suggested that this material has potential for use in spintronics.[31] Fe^{III} based 3D perovskites, $Cs_2M^IFe^{III}Cl_6$

[a]*New Chemistry Unit, International Centre for Materials Science, School of Advanced Materials, Jawaharlal Nehru Centre for Advanced Scientific Research, Jakkur P.O., Bangalore-560064, India. E-mail: pvishnoi@jncasr.ac.in*

[b]*School of Advanced Materials, Chemistry and Physics of Materials Unit, Jawaharlal Nehru Centre for Advanced Scientific Research (JNCASR), Jakkur P. O., Bangalore 560064, India*

† Electronic supplementary information (ESI) available: Synthesis, characterization methods, crystallographic information files (CIFs), PXRD patterns, XPS data, and additional figures of magnetic data. CCDC 2234517–2234521. For ESI and crystallographic data in CIF or other electronic format see DOI: https://doi.org/10.1039/d3sc00132f

© 2023 The Author(s). Published by the Royal Society of Chemistry

Open Access Article. Published on 06 March 2023. Downloaded on 1/11/2026 4:22:25 PM. This article is licensed under a Creative Commons Attribution-NonCommercial 3.0 Unported Licence.

(M^I = Na or Ag) have been reported as narrow bandgap semiconductors ($E_g = \sim 1.5$ eV),[32] as well as geometrically frustrating antiferromagnetic systems.[33] Ferromagnetic Cu^I–Cu^{II}–In^{III} based layered halide double perovskites have been recently reported.[34] Moving to 4d metals increases the importance of spin–orbit coupling (SOC) in exotic physics of unpaired spins such as magnetic frustration in layered α-$RuCl_3$,[35,36] α-$MoCl_3$,[37] and other heavy transition metal halides.[38] High SOC metal ions such as Ru^{III}, and Rh^{III} have been incorporated in 1-D chain,[39,40] and 2-D layered double perovskites.[41] The effect of SOC on the magnetic properties has been studied in these low dimensional systems. The Ru^{III} systems display unusual magnetic properties, particularly, deviation from the Kotani model for a low spin d^5 metal. By using the Kotani model, single ion magnetic properties of vacancy ordered double perovskites of Ru^{IV},[42] and Os^{IV},[43] both low spin d^4 ions, have been recently studied. These recent reports indeed suggest that transition metal based HDPs are of potential interest, which researchers have begun to explore.

In this work, we sought to introduce Mo^{III} ($4d^3$) as the magnetic ion into three new chloride based double perovskites: a 3-D rock-salt ordered $Cs_2NaMoCl_6$, a 1-D chain $(MA)_2AgMoCl_6$ and a 2-D layered $(1,4\text{-BDA})_2AgMoCl_8$ (where MA = methylammonium; 1,4-BDA = 1,4-butanediammonium). To our knowledge, $Cs_2NaMoCl_6$ is the first example of a chloride based 3-D HDP in which an open-shell 4d metal is incorporated at the B-site. Structurally, it is similar to prototype compound Sr_2FeMoO_6 which is one of the heavily discussed oxide perovskites in the condensed matter physics community in terms of unusual magnetic and electronic properties arising from the rock salt ordered sub-lattices of Fe^{III} (d^5) and Mo^V (d^1) ions.[44,45] $(MA)_2AgMoCl_6$ and $(1,4\text{-BDA})_2AgMoCl_8$ present rare examples of 1-D chain and 2-D layered hybrid double perovskites, respectively, in which both B^I and B^{III} metals are transition metal ions, *i.e.* Ag and Mo. We find that their structures are tuneable with different A-cations, *i.e.*, Cs, MA, and 1,4-BDA. Their optical and magnetic properties can be controlled with both chemical composition and structural dimensionality. Their X-ray structures, optical absorption, and magnetism are discussed below.

2. Results and discussion

2.1. Synthesis

The synthetic protocol for the compounds reported here is similar to the method reported in the literature by some of us (see the ESI for the method†).[39] Typically, to obtain $Cs_2NaMoCl_6$ and $(MA)_2AgMoCl_6$, a mixture of ACl (A = Cs or MA), B^ICl (B^I = Na or Ag) and $MoCl_3$ was heated hydrothermally in aqueous hydrochloric acid as the solvent. Crystals were obtained on slow cooling of the reaction autoclaves. Similarly, $(1,4\text{-BDA})_2AgMoCl_8$ was obtained from the reaction of 1,4-butanediamine, AgCl and $MoCl_3$. Initially in all the reactions, we observed the formation of a green solution likely stemming from the formation of higher valence Mo ions in aqueous HCl. A stoichiometric amount of H_3PO_2 (reducing agent) was used to control the oxidation. The structures of the as synthesized compounds were determined from single-crystal X-ray diffraction (SCXRD) data. Selected unit-cell parameters are given in Table 1 and the details in Tables S1–S5.† The selected bond parameters are given in Table S6.† The simulated powder X-ray diffraction (PXRD) patterns from the SCXRD data show a good match with the experimental PXRD patterns, confirming that all these compounds can be prepared as phase pure (Fig. S1–S3†).

2.2. Structure of $Cs_2NaMoCl_6$

As shown in Fig. 1, $Cs_2NaMoCl_6$ crystallizes in a cubic $Fm\bar{3}m$ space group, the 3D inorganic framework of which is composed of corner-shared $[NaCl_6]^{5-}$ and $[MoCl_6]^{3-}$ units at the B-site with rock-salt ordering. Locally, the Na^+ and Mo^{3+} ions form ideal octahedral units which are interconnected infinitely through Cl bridges along all three axes. The Cs^+ cation occupies the A-site interstitials. The Na–Cl (2.756(3) Å) and the Mo–Cl (2.450(3) Å) bond lengths are slightly shorter than those calculated (Na–Cl = 2.813 Å; Mo–Cl = 2.476 Å) from Shannon radii,[46] which is due to the increased covalency in the metal–halide bonds. Furthermore, a small displacement parameter (B_{eq}) of 2.16 in the case of a Cs cation, Cs^+ size to A-cavity size ratio of 0.99 and tolerance factor of 0.97 collectively suggest that the Cs^+ ion fits well in the A-site cavity. Perhaps, due to this reason, the compound shows high thermal and ambient stabilities (Fig. S4 and S5†).

2.3. Structure of $(MA)_2AgMoCl_6$

We, recently reported that a double perovskite most likely forms a corner-shared 3-D framework when the tolerance factor $\left(\mathrm{TF} = \frac{r_A + r_X}{\sqrt{2}[(r_{M^I} + r_{M^{III}})/2 + r_X]}\right)$ (where r_A, r_X, r_{M^I}, and $r_{M^{III}}$ are the radii of the A-cation, halide, monovalent metal and trivalent metal, respectively) is in the 0.8–1.0 range, and a face-shared 1-D chain when the TF is slightly more than 1.0.[47] Here, we

Table 1 Unit-cell parameters for $Cs_2NaMoCl_6$, $(MA)_2AgMoCl_6$, $(1,4\text{-BDA})_2AgMoCl_8$ and $(MA)_4MoCl_6\cdot Cl$

	$Cs_2NaMoCl_6$	$(MA)_2AgMoCl_6$	$(1,4\text{-BDA})_2AgMoCl_8$	$(1,4\text{-BDA})_2AgMoCl_8$_460 K	$(MA)_4MoCl_6\cdot Cl$
Space group	Cubic, $Fm\bar{3}m$	Trigonal, $P\bar{3}m1$	Triclinic, $P\bar{1}$	Triclinic, $P\bar{1}$	Monoclinic, $P2/n$
a (Å)	10.41290(10)	7.3359(2)	7.6668(15)	7.636(2)	16.0647(9)
b (Å)	10.41290(10)	7.3359(2)	7.7072(14)	7.671(2)	7.3477(4)
c (Å)	10.41290(10)	6.8017(2)	9.4490(14)	9.789(3)	16.1264(8)
α (°)	90	90	102.229(8)	80.191(12)	90
β (°)	90	90	91.183(6)	88.082(12)	103.599(2)
γ (°)	90	120	90.127(6)	89.402(12)	90
Volume (Å^3)	1129.05(3)	317.00(2)	545.54(17)	564.7(3)	1850.17(17)
CCDC number	2234517	2234518	2234519	2234520	2234521

Open Access Article. Published on 06 March 2023. Downloaded on 1/11/2026 4:22:25 PM.
This article is licensed under a Creative Commons Attribution-NonCommercial 3.0 Unported Licence.

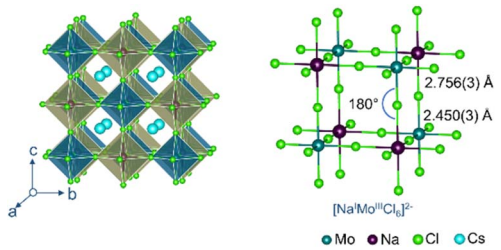

Fig. 1 SCXRD structure of $Cs_2NaMoCl_6$, and the ball and stick model of the corresponding perovskite frameworks is also provided to show corner-sharing connectivity of $[NaCl_6]^{5-}$ and $[MoCl_6]^{3-}$ units.

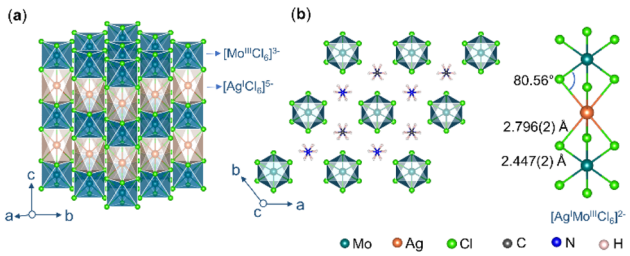

Fig. 2 SCXRD structure of $(MA)_2AgMoCl_6$: (a) side view and (b) top view. Ball and stick model of the corresponding perovskite framework is also provided to show face-sharing connectivity of $[AgCl_6]^{5-}$ and $[MoCl_6]^{3-}$ units.

Table 2 Bond distortion level (Δd) and bond angle variance (σ^2)

Compounds	Δd	σ^2
$Cs_2NaMoCl_6$	$[MoCl_6] = 0$	$[MoCl_6] = 0$
	$[NaCl_6] = 0$	$[NaCl_6] = 0$
$(MA)_2AgMoCl_6$	$[MoCl_6] = 0$	$[MoCl_6] = 0.6136$
	$[AgCl_6] = 0$	$[AgCl_6] = 217.49$
$(1,4\text{-BDA})_2AgMoCl_8$	$[MoCl_6] = 1.03 \times 10^{-6}$	$[MoCl_6] = 0.5047$
	$[AgCl_6] = 9.85 \times 10^{-3}$	$[AgCl_6] = 6.448$
$(MA)_4MoCl_6 \cdot Cl$	$[MoCl_6] = 1.59 \times 10^{-6}$	$[MoCl_6] = 0.1609$
	$[MoCl_6] = 1.48 \times 10^{-7}$	$[MoCl_6] = 0.0979$

replaced Cs^+ with MA and Na^+ with Ag^+ to obtain $(MA)_2AgMoCl_6$ (Fig. 2a and b) which has a TF of 1.03. It crystallizes in a hexagonal phase, similar to previously reported Ag^I–Ru^{III} halide perovskites.[39] The $[AgCl_6]^{5-}$ and $[MoCl_6]^{3-}$ octahedra are alternatively connected by face-sharing of two opposite faces in 1-D chain running along the *c*-axis. The MA cation occupies the interchain space and forms N···H···Cl hydrogen bonds with chlorides (the shortest N···Cl distance of 3.37 Å). It is worthwhile to note that both $[MoCl_6]^{3-}$ and $[AgCl_6]^{5-}$ octahedra are trigonally distorted, with the latter being heavily distorted as suggested by the bond angle variance (σ^2) (Table 2).

2.4. Structure of $(1,4\text{-BDA})_2AgMoCl_8$

Layers of 2-D perovskite can be thought of as derived from slicing (conceptually) the 3-D analogue along a specific crystallographic plane and stacking the slices over each other when large organic ammonium is used as the A-cation.[48] We used 1,4-BDA to obtain $(1,4\text{-BDA})_2AgMoCl_8$ which crystallizes in a triclinic $P\bar{1}$ space group as a (100)-oriented Dion–Jacobson (DJ) type double perovskite (Fig. 3a). The perovskite layer is composed of orderly arranged $[AgCl_6]^{5-}$ and $[MoCl_6]^{3-}$ in the *ab*-plane which are inter-connected through four equatorial chlorides, while two axial chlorides remain dangling in the interlayer space (Fig. 3b). The [0,0] type of layer stacking pattern is clearly distinguishable without stacking-fault or without mixed stacking of Ag^I/Ag^I and Ag^I/Mo^{III} phases.[49] The $[AgCl_6]^{5-}$ polyhedra are highly distorted which is commonly ascribed to preferential formation of linear coordination geometry due to the mixing of filled Ag 4d orbitals with empty Ag 5s orbitals.[50] The 1,4-BDA spacer adopts a *gauche* conformation (Fig. 3c). Our previous studies have revealed that the *gauche* conformation of this spacer is stable in layered Ag–Ru–Br perovskite, $(1,4\text{-BDA})_2AgRuBr_8$ and the *anti* conformation, in layered Ag–Ru–Cl perovskite, $(1,4\text{-BDA})_2AgRuCl_8$ at room temperature.[41] Here, we show that this spacer can exhibit both *gauche* and *anti* conformations in the same compound, but at different temperatures. The calorimetric measurements suggest a reversible phase transition (Fig. 3d) and the SCXRD structure confirms that the phase transition is driven by a *gauche* ⇋ *anti* conformational change. In a 460 K structure (Fig. 3e), half the number of 1,4-BDA cations have changed from the *gauche* (Fig. 3f) form to the *anti* (Fig. 3g) form without changing the overall lattice symmetry and the compound formula can therefore be written as [(*gauche*-1,4-BDA)(*anti*-1,4-BDA)]$AgMoCl_8$. There is a slight volume expansion due to the increase in the interlayer distance. The octahedral tilting in the perovskite layer is slightly reduced (Fig. 3h). As shown in Fig. S6 and S7,† the perovskite layer has cavities of two different sizes and two crystallographically different 1,4-BDA cations. The BDA-2 which forms N–H···Cl hydrogen bonds with the chlorides of the larger cavity is more disordered with larger thermal parameters in the room temperature as well as in the high temperature structures. Furthermore, BDA-2 is found to be longer with more penetration depth below the plane of axial chlorides. We believe that BDA-2 changes the conformation from *gauche* to *anti* during the phase transition, whilst BDA-1 remains quiet. We did not observe significant changes in the N···Cl distances as a consequence of the change in the 1,4-BDA conformation (Table S7†).

2.5. XPS

It is important to note that Mo is susceptible to oxidation and can therefore exist in multiple oxidation states under ambient conditions. We measured X-ray photoelectron spectroscopy (XPS) spectra to examine the chemical composition as well as the valence state of Mo ions (Fig. S9–S14 and Table S8†). The spectra show the presence of the desired elements. The core level Mo 3d spectra exhibit characteristic doublet peaks at around 229 eV and 232 eV with a peak area ratio of 3 : 2, corresponding to the Mo $3d_{5/2}$ and Mo $3d_{3/2}$ states (Fig. 4). These binding energies and the peak area ratios clearly suggest that the Mo is in the trivalent state in all these compounds.[51] Furthermore, we did not observe any

 © 2023 The Author(s). Published by the Royal Society of Chemistry

Open Access Article. Published on 06 March 2023. Downloaded on 1/11/2026 4:22:25 PM.
This article is licensed under a Creative Commons Attribution-NonCommercial 3.0 Unported Licence.

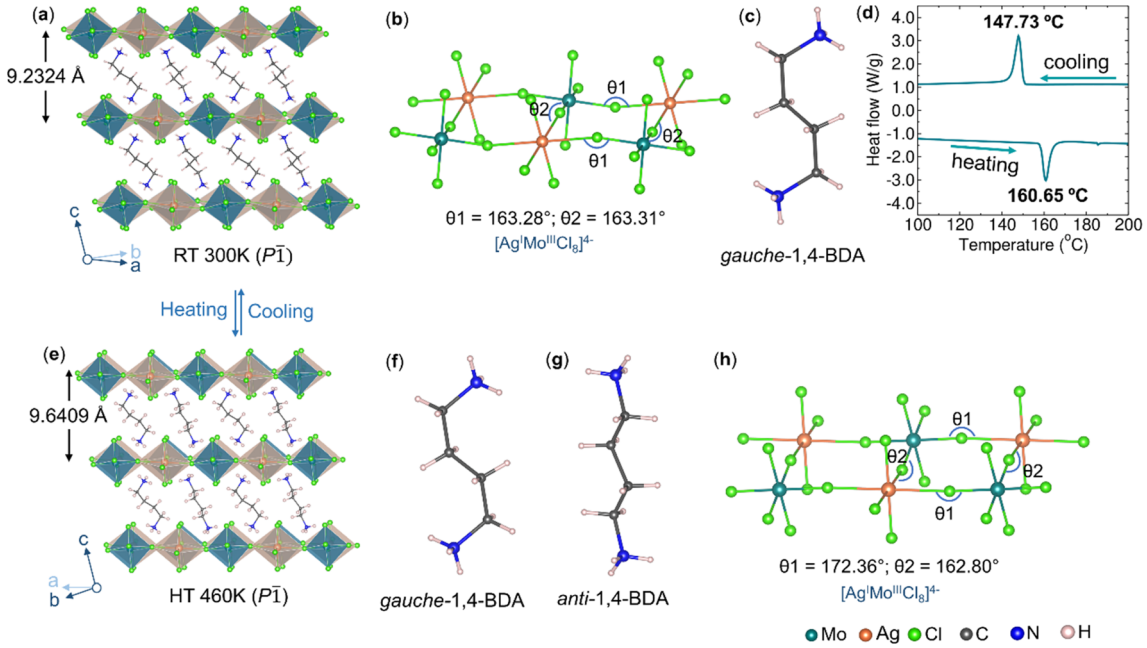

Fig. 3 (a) Room temperature SCXRD structure of $(1,4\text{-BDA})_2AgMoCl_8$. (b) Corresponding ball and stick models for the perovskite layer showing octahedral connectivity between $[AgCl_6]^{5-}$ and $[MoCl_6]^{3-}$ units. (c) 1,4-BDA spacer in a *gauche* conformation. (d) DSC curve of $(1,4\text{-BDA})_2AgMoCl_8$. (e) SCXRD structure of $(1,4\text{-BDA})_2AgMoCl_8$ at 460 K. (f and g) 1,4-BDA spacer in *gauche* and *anti* conformations. (h) Ball and stick models for the perovskite layer in the 460 K structure, showing reduced octahedral tilting than that of the room temperature structure.

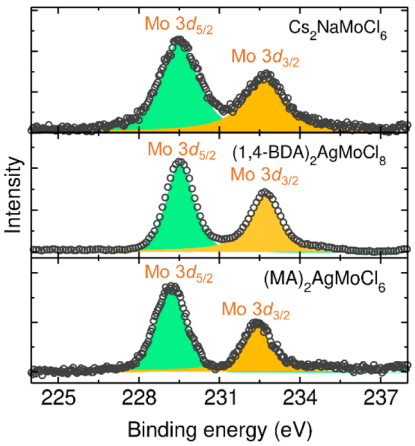

Fig. 4 Core level XPS spectra of Mo 3d states.

Mo 3d peaks at higher binding energies, confirming the absence of higher valence states.

2.6. UV-visible absorption spectra

Fig. 5a shows the UV-visible absorption spectra of these double perovskites which were recorded in the reflectance mode and converted to absorbance by using the Kubelka–Munk formula $[\alpha/S = (1-R)^2/(2R)]$ (where α, S, and R represent the absorption coefficient, scattering coefficient, and absolute reflectance, respectively). The spectra suggest that the optical bandgap increases in the order of $Cs_2NaMoCl_6$ (E_g = 2.0 eV), $(1,4\text{-BDA})_2AgMoCl_8$ (E_g = 2.04 eV) and $(MA)_2AgMoCl_6$ (E_g = 2.12 eV). We attribute this bandgap blueshift to the reduced orbital overlap caused by both reduced dimensionality and increased structural distortion (Fig. 5b).[14] However, the bandgap shift is minute between the 3-D and the 2-D compounds, which is likely due to the increased bandgap of the former compound as a consequence of poor contribution of Na to the electronic band near the extrema when compared to that of Ag.[52] As listed in Table 2, $(MA)_2AgMoCl_6$ has the highest bond angle variance (σ^2),[53] indicating a high octahedral distortion which correlates well with its higher value of bandgap. Furthermore, the dimensionality control of the bandgap shift is undoubtedly clear in the case of the 2-D and the 1-D phases, wherein the chemical constituents of the perovskite frameworks are identical, *e.g.*, Ag and Mo at the B-site. However, the magnitude of the bandgap shift is smaller than those observed in post-transition-metal analogues. Furthermore, the bandgaps are smaller than those of heavily explored halide double perovskites $Cs_2AgBiBr_6$ (E_g = 2.17 eV),[4] $Cs_2AgBiCl_6$ (E_g = 2.77 eV),[4] and $Cs_2AgInCl_6$ (E_g = 3.2 eV).[54] We also observed a weak band at low energy in each spectrum which is consistent with the spin forbidden $^4A_{2g} \rightarrow {}^4T_{1g}$ transitions in Mo^{III} chloride.[55]

2.7. Magnetism

We measured magnetic susceptibility (χ) for all the three perovskites in the temperature range of 2 K to 300 K by using a superconducting quantum interference device-vibrating sample magnetometer (SQUID-VSM). The susceptibility data were fitted to the modified Curie–Weiss law equation $[\chi = C/(T - \theta_{CW}) + \chi_0]$, where C is the Curie constant which is proportional to the square of the effective magnetic moment

Open Access Article. Published on 06 March 2023. Downloaded on 1/11/2026 4:22:25 PM.
This article is licensed under a Creative Commons Attribution-NonCommercial 3.0 Unported Licence.

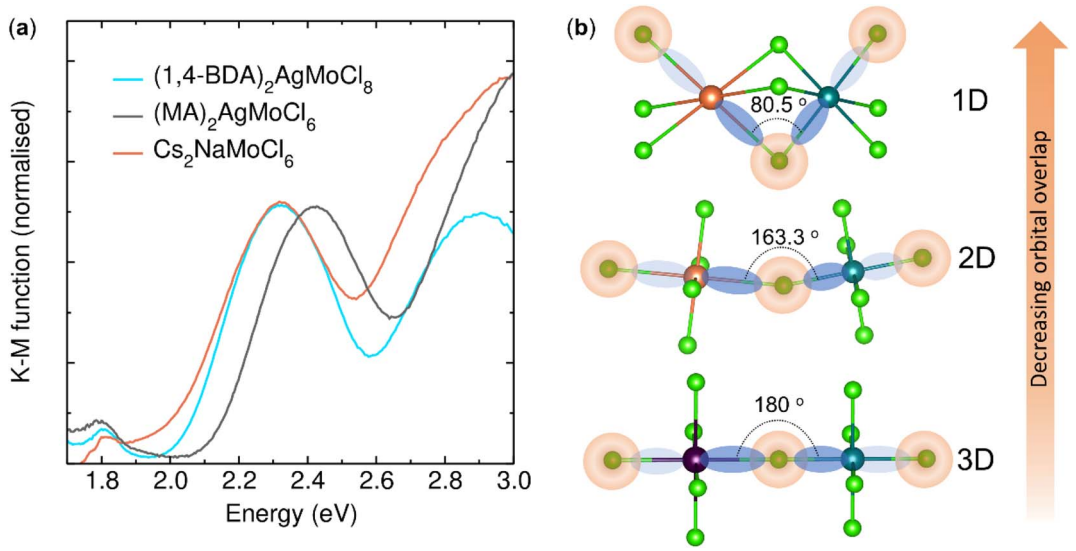

Fig. 5 (a) Optical absorption spectra. (b) Schematic illustration of reduced orbital overlapping between $[M^{I}Cl_6]^{5-}$ and $[Mo^{III}Cl_6]^{3-}$ octahedra due to lattice distortion.

($\mu_\beta = \sqrt{8C}$), T is the temperature, θ_{CW} is the Curie–Weiss temperature which is a measure of the strength and the nature of magnetic exchange interaction between the nearest-neighbors, and χ_0 is the temperature-independent diamagnetic contribution. Fig. 6a and b show the molar susceptibility curves. We shall first discuss the magnetic properties of $Cs_2NaMoCl_6$

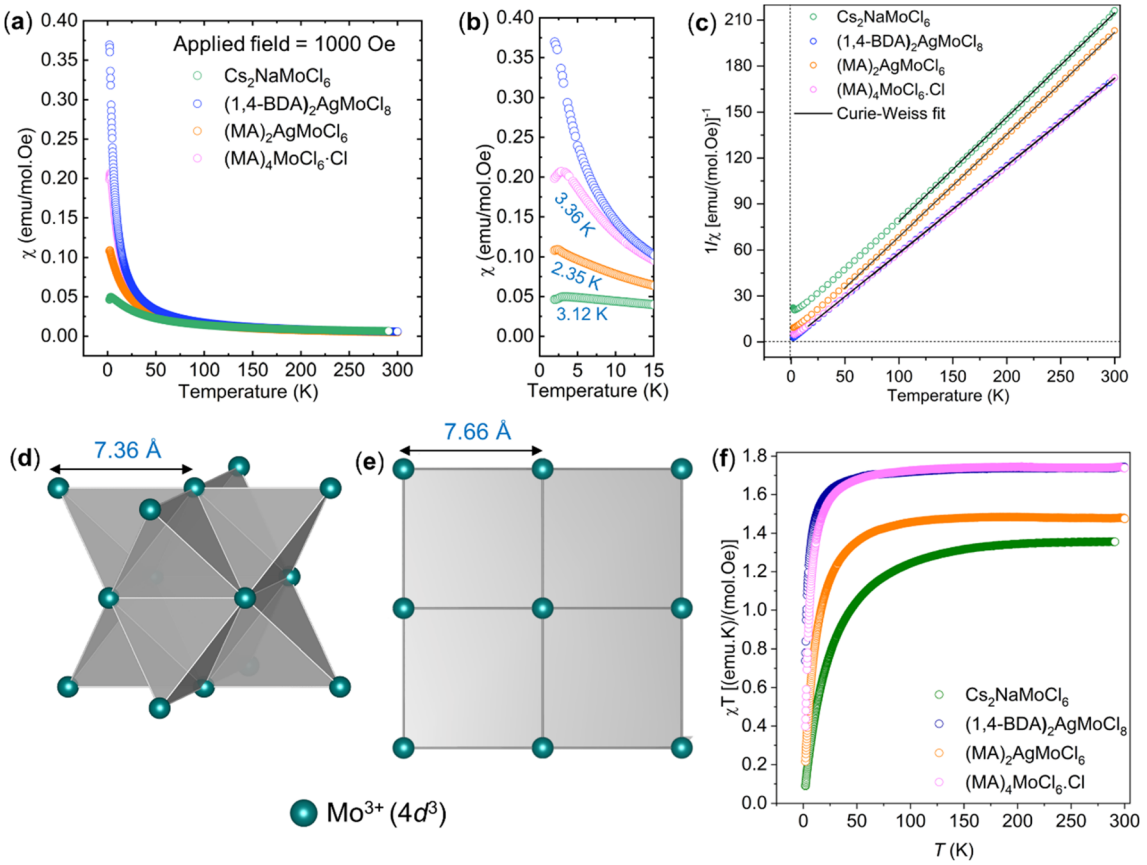

Fig. 6 (a and b) Temperature dependent magnetic susceptibility curves. (c) Curie–Weiss fitting of the susceptibility data shown in panel (a). (d) Geometrically frustrating tetrahedron based on Mo^{3+} ions in $Cs_2NaMoCl_6$. (e) Square lattice based on Mo^{3+} ions in $(1,4\text{-BDA})_2AgMoCl_8$. (f) Thermal dependence of the $\chi_M T$ products.

 © 2023 The Author(s). Published by the Royal Society of Chemistry

Open Access Article. Published on 06 March 2023. Downloaded on 1/11/2026 4:22:25 PM.
This article is licensed under a Creative Commons Attribution-NonCommercial 3.0 Unported Licence.

which exhibits long range antiferromagnetic ordering at a Néel temperature (T_N) of 3.12 K, and there is no divergence in zero field cooled (ZFC) and field cooled (FC) curves (Fig. S16†). Above T_N, the paramagnetic susceptibility shows an excellent fit to the Curie–Weiss equation with a negative Curie–Weiss temperature (θ_{CW}) of −15.8 K, and Curie constant (C) of 1.472 emu Oe^{-1} K mol^{-1} (Fig. 6c). The effective magnetic moment μ_β is calculated to be 3.43 μ_B f.u.$^{-1}$ which is slightly less than the spin only moment of 3.87 μ_B f.u.$^{-1}$ for a d^3 ion [$\mu_\beta = \sqrt{n(n+2)}$, where n = number of unpaired electrons, $n = 3$ in this case]. Fig. 6d shows the fcc sub-lattice composed of magnetic Mo ions in $Cs_2NaMoCl_6$ which clarifies the edge-shared tetrahedral arrangement of Mo^{3+} metal ions in a geometrically frustrating system. The tetrahedron is dimensionally symmetric with a nearest-neighbor Mo···Mo separation of 7.36 Å. The calculated magnetic frustration index $f\left(f = \frac{|\theta_{CW}|}{T_N}\right)$ of 5.0 indeed suggests that the system has weak magnetic frustration, and it warrants further studies.[56,57] The 1-D compound $(MA)_2AgMoCl_6$ features an antiferromagnetic transition temperature T_N of 2.35 K and a negative θ_{CW} of −2.9 K with an effective magnetic moment of 3.48 μ_B f.u.$^{-1}$ The calculated frustration index (f) of 1.2 indicates that this 1-D system is magnetically non-frustrating.

In the case of $(1,4\text{-BDA})_2AgMoCl_8$, we did not observe magnetic ordering down to the lowest measurement temperature of 2 K, but the system obeys the Curie–Weiss law. Only a weak antiferromagnetic exchange was observed with a θ_{CW} of −1.7 K and an effective moment of 3.74 μ_B f.u.$^{-1}$ We attribute the weakening of AFM exchange to the increased distance between the nearest-neighbor spins (Mo···Mo = 7.667 Å) compared to that in $Cs_2NaMoCl_6$ (7.363 Å) and $(MA)_2AgMoCl_6$ (6.802 Å). The geometric frustration has also significantly relaxed in the 2D system due to the formation of a square lattice (Fig. 6e). The isothermal field dependent M–H curve (Fig. S20c†) of $(1,4\text{-BDA})_2AgMoCl_8$ at 2 K adopts a non-linear shape, but with no hysteresis (neither remanence nor coercivity), suggesting paramagnetic behaviour.[58] The M–H loops (Fig. S20a and b†) of $Cs_2NaMoCl_6$ and $(MA)_2AgMoCl_6$ are linear which is characteristic of an antiferromagnetic nature. Additionally, we synthesized $(MA)_4MoCl_6\cdot Cl$ (Fig. S21†), a molecular compound, with a nearest-neighbor Mo···Mo distance of 7.35 Å which is close to that found in $Cs_2NaMoCl_6$ (7.363 Å). Also, it shows a T_N of 3.36 K, close to that of $Cs_2NaMoCl_6$, but the strength of AFM coupling is much weaker as indicated by a θ_{CW} of −1.2 K. This suggests that the magnetic coupling in these systems primarily takes place through the –Mo^{III}–Cl–M^{I}–Cl–Mo^{III}– pathway, the strength of which depends not only on the nearest-neighbor Mo···Mo distance, but also on the geometry of the magnetic sub-lattice. Fig. 6f shows that on lowering the temperature, $\chi_M T$ values decrease which indicates antiferromagnetic interactions in all these systems.

3. Conclusions

In summary, we have synthesized and structurally characterized three new chloride double perovskites with Na^+/Ag^+ and Mo^{3+} metal ions ordering at the perovskite B-site. The X-ray structures suggest that octahedral connectivity and dimensionality of the inorganic sub-lattice can readily be modulated with the choice of the A-site cation. The measured bandgaps are relatively narrow (2.0–2.1 eV) which are even lower than that of the benchmark double perovskite $Cs_2AgBiBr_6$ (2.2 eV), and are tuneable with structural dimensionality. Magnetic measurements suggest nearest-neighbor antiferromagnetic coupling at low temperatures which occurs due to super-exchange through the –Mo^{III}–Cl–M^{I}–Cl–Mo^{III}– (M^{I} = Na or Ag) pathway. The magnetic ordering parameters, the Curie–Weiss temperature (θ_{CW}) and the Néel temperature (T_N) can be tuned with the dimensionality of the magnetic sub-lattice. In the case of 3-D perovskite, $|\theta_{CW}| \gg T_N$ suggests magnetic frustration as a consequence of the fcc arrangement of Mo^{3+} (4d^3) ion, whilst the 1-D and 2-D analogues do not exhibit such an arrangement. These materials expand the scope of halide double perovskites beyond optoelectronics, and we hope that these results will trigger future developments in magnetic optoelectronic halide perovskites by making use of other A-site cations, B-site metals and halides.

Data availability

Crystallographic information files have been deposited in CCDC (2234517–2234521). All necessary supporting data are provided in the ESI.†

Author contributions

DCB: carried out the experiments, data analysis (except magnetic data), wrote the initial draft of manuscript. PPM and DPP: magnetic data collection and analysis. PV: project design, conceptualization, methodology, data curation, manuscript writing and revision, project administration, and funding acquisition.

Conflicts of interest

Authors declare no conflict of interest.

Acknowledgements

The authors thank Prof. C. N. R. Rao (FRS) for his kind support and guidance. This work was financially supported by the Science & Engineering Research Board (SERB) of the Govt. of India through a Ramanujan Fellowship (Grant No. RJF/2020/000106), and a Core Research Grant (Grant No. CRG/2022/009230) to PV. We thank the SERB for these grants and the Jawaharlal Nehru Centre for Advanced Scientific Research (JNCASR), Bangalore, for the research infrastructure. PV also thanks the Sheikh Saqr Laboratory (SSL) for financial support. DCB thanks JNCASR and SSL for fellowships. DPP thanks CSIR for fellowship.

Open Access Article. Published on 06 March 2023. Downloaded on 1/11/2026 4:22:25 PM.
This article is licensed under a Creative Commons Attribution-NonCommercial 3.0 Unported Licence.

Notes and references

1 A. H. Slavney, T. Hu, A. M. Lindenberg and H. I. Karunadasa, *J. Am. Chem. Soc.*, 2016, **138**, 2138–2141.
2 G. Ji and Z. Xiao, *Chem. Mater.*, 2022, **34**, 8207–8212.
3 X.-G. Zhao, J.-H. Yang, Y. Fu, D. Yang, Q. Xu, L. Yu, S.-H. Wei and L. Zhang, *J. Am. Chem. Soc.*, 2017, **139**, 2630–2638.
4 E. T. McClure, M. R. Ball, W. Windl and P. M. Woodward, *Chem. Mater.*, 2016, **28**, 1348–1354.
5 G. Volonakis, M. R. Filip, A. A. Haghighirad, N. Sakai, B. Wenger, H. J. Snaith and F. Giustino, *J. Phys. Chem. Lett.*, 2016, **7**, 1254–1259.
6 J. Zhou, X. Rong, M. S. Molokeev, X. Zhang and Z. Xia, *J. Mater. Chem. A*, 2018, **6**, 2346–2352.
7 H. Lei, D. Hardy and F. Gao, *Adv. Funct. Mater.*, 2021, **31**, 2105898.
8 A. Noculak, V. Morad, K. M. McCall, S. Yakunin, Y. Shynkarenko, M. Wörle and M. V. Kovalenko, *Chem. Mater.*, 2020, **32**, 5118–5124.
9 F. Igbari, R. Wang, Z.-K. Wang, X.-J. Ma, Q. Wang, K.-L. Wang, Y. Zhang, L.-S. Liao and Y. Yang, *Nano Lett.*, 2019, **19**, 2066–2073.
10 J. A. Steele, W. Pan, C. Martin, M. Keshavarz, E. Debroye, H. Yuan, S. Banerjee, E. Fron, D. Jonckheere, C. W. Kim, W. Baekelant, G. Niu, J. Tang, J. Vanacken, M. Van der Auweraer, J. Hofkens and M. B. J. Roeffaers, *Adv. Mater.*, 2018, **30**, 1804450.
11 F. Fang, H. Li, S. Fang, B. Zhou, F. Huang, C. Ma, Y. Wan, S. Jiang, Y. Wang, B. Tian and Y. Shi, *Adv. Opt. Mater.*, 2021, **9**, 2001930.
12 Z. Weng, J. Qin, A. A. Umar, J. Wang, X. Zhang, H. Wang, X. Cui, X. Li, L. Zheng and Y. Zhan, *Adv. Funct. Mater.*, 2019, **29**, 1902234.
13 X.-G. Zhao, D. Yang, J.-C. Ren, Y. Sun, Z. Xiao and L. Zhang, *Joule*, 2018, **2**, 1662–1673.
14 Z. Xiao, W. Meng, J. Wang, D. B. Mitzi and Y. Yan, *Mater. Horiz.*, 2017, **4**, 206–216.
15 E. Alter and R. Hoppe, *Z. Anorg. Allg. Chem.*, 1975, **412**, 110–120.
16 G. Siebert and R. Hoppe, *Z. Anorg. Allg. Chem.*, 1972, **391**, 117–125.
17 E. Alter and R. Hoppe, *Z. Anorg. Allg. Chem.*, 1974, **403**, 127–136.
18 E. Alter and R. Hoppe, *Z. Anorg. Allg. Chem.*, 1974, **407**, 305–312.
19 E. Alter and R. Hoppe, *Z. Anorg. Allg. Chem.*, 1974, **405**, 167–175.
20 R. Hoppe and K. Lehr, *Z. Anorg. Allg. Chem.*, 1975, **416**, 240–250.
21 L. M. Toth, G. D. Brunton and G. P. Smith, *Inorg. Chem.*, 1969, **8**, 2694–2697.
22 V. Wilhelm and R. Hoppe, *Z. Anorg. Allg. Chem.*, 1975, **414**, 91–96.
23 R. Acevedo and V. Poblete, *Powder Diffr.*, 1995, **10**, 241–242.
24 M. E. Villafuerte-Castrejón, M. R. Estrada, J. Gómez-Lara, J. Duque and R. Pomés, *J. Solid State Chem.*, 1997, **132**, 1–5.
25 L. Mao, J. Chen, P. Vishnoi and A. K. Cheetham, *Acc. Mater. Res.*, 2022, **3**, 439–448.
26 J. Wang, C. Zhang, H. Liu, R. McLaughlin, Y. Zhai, S. R. Vardeny, X. Liu, S. McGill, D. Semenov, H. Guo, R. Tsuchikawa, V. V. Deshpande, D. Sun and Z. V. Vardeny, *Nat. Commun.*, 2019, **10**, 129.
27 L. T. Nguyen and R. J. Cava, *Chem. Rev.*, 2021, **121**, 2935–2965.
28 L. A. Muscarella and E. M. Hutter, *ACS Energy Lett.*, 2022, **7**, 2128–2135.
29 S. Thawarkar, S. R. Rondiya, N. Y. Dzade, N. Khupse and S. Jadkar, *Chem.–Eur. J.*, 2021, **27**, 7408–7417.
30 Z. Zhang, G. Liu, W. Guo, X. Li, Y. Zhang, C. Wu, B. Qu, J. Shi, Z. Chen and L. Xiao, *Mater. Adv.*, 2022, **3**, 4932–4937.
31 W. Ning, J. Bao, Y. Puttisong, F. Moro, L. Kobera, S. Shimono, L. Wang, F. Ji, M. Cuartero, S. Kawaguchi, S. Abbrent, H. Ishibashi, R. De Marco, I. A. Bouianova, G. A. Crespo, Y. Kubota, J. Brus, D. Y. Chung, L. Sun, W. M. Chen, M. G. Kanatzidis and F. Gao, *Sci. Adv.*, 2020, **6**, eabb5381.
32 H. Yin, Y. Xian, Y. Zhang, W. Chen, X. Wen, N. U. Rahman, Y. Long, B. Jia, J. Fan and W. Li, *Adv. Funct. Mater.*, 2020, **30**, 2002225.
33 J. Xue, Z. Wang, A. Comstock, Z. Wang, H. H. Y. Sung, I. D. Williams, D. Sun, J. Liu and H. Lu, *Chem. Mater.*, 2022, **34**, 2813–2823.
34 B. A. Connor, R. W. Smaha, J. Li, A. Gold-Parker, A. J. Heyer, M. F. Toney, Y. S. Lee and H. I. Karunadasa, *Chem. Sci.*, 2021, **12**, 8689–8697.
35 S. Mashhadi, Y. Kim, J. Kim, D. Weber, T. Taniguchi, K. Watanabe, N. Park, B. Lotsch, J. H. Smet, M. Burghard and K. Kern, *Nano Lett.*, 2019, **19**, 4659–4665.
36 A. Banerjee, C. A. Bridges, J.-Q. Yan, A. A. Aczel, L. Li, M. B. Stone, G. E. Granroth, M. D. Lumsden, Y. Yiu, J. Knolle, S. Bhattacharjee, D. L. Kovrizhin, R. Moessner, D. A. Tennant, D. G. Mandrus and S. E. Nagler, *Nat. Mater.*, 2016, **15**, 733–740.
37 M. A. McGuire, J. Yan, P. Lampen-Kelley, A. F. May, V. R. Cooper, L. Lindsay, A. Puretzky, L. Liang, S. KC, E. Cakmak, S. Calder and B. C. Sales, *Phys. Rev. Mater.*, 2017, **1**, 64001.
38 H. Lu, J. R. Chamorro, C. Wan and T. M. McQueen, *Inorg. Chem.*, 2018, **57**, 14443–14449.
39 P. Vishnoi, J. L. Zuo, T. A. Strom, G. Wu, S. D. Wilson, R. Seshadri and A. K. Cheetham, *Angew. Chem., Int. Ed.*, 2020, **59**, 8974–8981.
40 N. P. Holzapfel, A. Milder and P. M. Woodward, *Chem. Mater.*, 2022, **34**, 7705–7711.
41 P. Vishnoi, J. L. Zuo, X. Li, D. C. Binwal, K. E. Wyckoff, L. Mao, L. Kautzsch, G. Wu, S. D. Wilson, M. G. Kanatzidis, R. Seshadri and A. K. Cheetham, *J. Am. Chem. Soc.*, 2022, **144**, 6661–6666.
42 P. Vishnoi, J. L. Zuo, J. A. Cooley, L. Kautzsch, A. Gómez-Torres, J. Murillo, S. Fortier, S. D. Wilson, R. Seshadri and A. K. Cheetham, *Angew. Chem., Int. Ed.*, 2021, **60**, 5184–5188.
43 M. Saura-Múzquiz, M. Avdeev, H. E. A. Brand and B. J. Kennedy, *Inorg. Chem.*, 2022, **61**, 15961–15972.

 © 2023 The Author(s). Published by the Royal Society of Chemistry

Open Access Article. Published on 06 March 2023. Downloaded on 1/11/2026 4:22:25 PM.
This article is licensed under a Creative Commons Attribution-NonCommercial 3.0 Unported Licence.

44 D. D. Sarma, E. V. Sampathkumaran, S. Ray, R. Nagarajan, S. Majumdar, A. Kumar, G. Nalini and T. N. Guru Row, *Solid State Commun.*, 2000, **114**, 465–468.
45 A. Arulraj, K. Ramesha, J. Gopalakrishnan and C. N. R. Rao, *J. Solid State Chem.*, 2000, **155**, 233–237.
46 R. D. Shannon, *Acta Crystallogr., Sect. A: Cryst. Phys., Diffr., Theor. Gen. Crystallogr.*, 1976, **32**, 751–767.
47 P. Vishnoi, R. Seshadri and A. K. Cheetham, *J. Phys. Chem. C*, 2021, **125**, 11756–11764.
48 X. Li, J. M. Hoffman and M. G. Kanatzidis, *Chem. Rev.*, 2021, **121**, 2230–2291.
49 B. Vargas, G. Rodríguez-López and D. Solis-Ibarra, *ACS Energy Lett.*, 2020, **5**, 3591–3608.
50 R. Hooijer, A. Weis, A. Biewald, M. T. Sirtl, J. Malburg, R. Holfeuer, S. Thamm, A. A. Y. Amin, M. Righetto, A. Hartschuh, L. M. Herz and T. Bein, *Adv. Opt. Mater.*, 2022, **10**, 2200354.
51 Z. Wang, Y. Han, J. Liang, H. Huang, C. Hu, P. Liu, J. Xiang, Z. Qi, Y. Lu, K. Liu, J. Jiang and B. Xiang, *ACS Appl. Electron. Mater.*, 2020, **2**, 2678–2684.
52 R. S. Lamba, P. Basera, S. Bhattacharya and S. Sapra, *J. Phys. Chem. Lett.*, 2019, **10**, 5173–5181.
53 K. Robinson, G. V. Gibbs and P. H. Ribbe, *Science*, 1971, **172**, 567–570.
54 J. Luo, S. Li, H. Wu, Y. Zhou, Y. Li, J. Liu, J. Li, K. Li, F. Yi, G. Niu and J. Tang, *ACS Photonics*, 2018, **5**, 398–405.
55 R. V. Kamalov, V. A. Volkovich, I. B. Polovov and B. D. Vasin, *Russ. Metall.*, 2012, **2012**, 114–118.
56 H. Karunadasa, Q. Huang, B. G. Ueland, P. Schiffer and R. J. Cava, *Proc. Natl. Acad. Sci. U. S. A.*, 2003, **100**, 8097–8102.
57 S. Mugiraneza and A. M. Hallas, *Commun. Phys.*, 2022, **5**, 95.
58 A. Lodi Rizzini, C. Krull, T. Balashov, A. Mugarza, C. Nistor, F. Yakhou, V. Sessi, S. Klyatskaya, M. Ruben, S. Stepanow and P. Gambardella, *Nano Lett.*, 2012, **12**, 5703–5707.

© 2023 The Author(s). Published by the Royal Society of Chemistry